This article has been accepted for publication in a future issue of this journal, but has not been fully edited. Content may change prior to final publication. Citation information: DOI10.1109/JIOT.2024.3448350,

Time-Frequency Hybrid Neuromorphic Computing Architecture Development for Battery State-of-Health Estimation

Xiaoyue Ji, *Member, IEEE*, Yi Chen, Junfan Wang, *Student Member, IEEE*, Guangdong Zhou, Chun Sing Lai, *Senior Member, IEEE*, *Zhekang Dong, Senior Member, IEEE*

***Abstract*—With the rapid adoption of Internet of things (IoT) and artificial intelligence (AI), lithium-ion battery state-of-health (SOH) estimation plays an important role in guaranteeing the secure and stable functioning of various domains. However, the majority of the existing methods are constrained by factors such as transmission latency, computational energy, and computing speed. To address these challenges, we develop a time-frequency hybrid neuromorphic computing architecture for battery SOH estimation. Specifically, an eco-friendly, biodegradable memristor crossbar array is designed, enabling high energy efficiency and high-performance density in the proposed system. To improve the understanding of the designed time-frequency hybrid neuromorphic computing system, a local information extraction module, a time-frequency feature fusion module, and a global information perception module are proposed. Furthermore, the proposed system is validated on two publicly available battery ageing datasets (i.e., the CALCE-CS2 dataset and the NASA dataset). The experimental results show that the system exhibits superior performance to that of the state-of-the-art (SOTA) methods in terms of estimation accuracy (highest estimation accuracy), time consumption (approximately 8~12 times faster), and transmission latency (approximately 10 times faster). This study is expected to promote the advancement and evolution of next-generation computing systems, enabling the realization of low power consumption and high-density information processing in IoT scenarios.**

***Index Terms*—Neuromorphic computing, circuit design, memristor, lithium-ion battery, state-of-health estimation**

Manuscript received June 27, 2024.

X. Ji and Y. Chen contributed equally to this work.

This work was supported in part by the Postdoctoral Fellowship Program of CPSF under Grant GZB20230356, the Shuimu Tsinghua Scholar program under Grant 2023SM035, the National Natural Science Foundation of China under Grant 62206062, and the Fundamental Research Funds for the Provincial University of Zhejiang under Grant GK229909299001-06. *(Corresponding author: Zhekang Dong).*

X. Ji is with the Ocean College, Zhejiang University, Hangzhou 310027, China and with the Department of Precision Instrument, Tsinghua University, Beijing 100084, China. (e-mail: jixiaoyue@mail.tsinghua.edu.cn).

Y. Chen is with the Ocean College, Zhejiang University, Hangzhou 310027, China (e-mail: morningone@126.com).

J. Wang, and Z. Dong are with the School of Electronics and Information, Hangzhou Dianzi University, Hangzhou 310018, China, and with the Zhejiang Provincial Key Lab of Equipment Electronics, Hangzhou 310018, China (e-mail: wangjunfan@hdu.edu.cn; englishp@hdu.edu.cn).

G. Zhou is with the College of Artificial Intelligence, Southwest University, Chongqing 400715, China (e-mail: zhougd@swu.edu.cn).

C. S. Lai is with the Department of Electronic and Electrical Engineering, Brunel University London, London, UB8 3PH, UK and with the School of Automation, Guangdong University of Technology, Guangzhou, China 510006 (email: chunsing.lai@brunel.ac.uk).

I. Introduction

Lithium-ion batteries, which serve as crucial energy storage devices, have been widely used across various domains, from Internet of Things (IoT)-embedded devices and portable electronics in daily life to renewable energy equipment in intelligent transportation scenarios and smart cities [1]. Regardless of the application, lithium-ion batteries degrade over time, and this degradation process is influenced by complex operating conditions, charging/discharging rates, and other influencing factors [2]. Accurately estimating battery degradation irrespective of the degradation path and various failure mechanisms is an urgent need for battery management systems [3]. Therefore, state-of-health (SOH) estimation, which can reflect battery degradation trends and reliability, has been extensively studied in recent years [4].

In general, SOH estimation approaches can be roughly divided into the following three categories: electrochemical methods, equivalent circuit methods, and data-driven methods [5, 6]. Electrochemical methods rely on accurately modelling the electrochemical processes occurring inside a battery, resulting in substantial computational cost and computing memory requirements [7-8]. Compared to electrochemical methods, equivalent circuit methods, which require fewer inputs, greatly reduce the incurred computational cost but have certain limitations in terms of estimation accuracy and robustness [9-11]. With the rapid development of big data and artificial intelligence (AI), data-driven methods have achieved high estimation accuracy without complex electrochemical modelling processes [12-18]. However, data-driven methods are typically energy-intensive computing techniques and are implemented by the von Neumann computing architecture. The extensive shuffling of data between the processing unit and memory unit leads to significant energy consumption and constitutes the majority of the latency in power-limited IoT scenarios.

A promising alternative is memristor-based neuromorphic computing, which circumvents extensive data movements through its integrated memory processing architectures, providing a potential solution to the bottleneck that is inherent in von Neumann architectures [21]. Memristor-based neuromorphic computing systems that integrate complementary metal-oxide semiconductor (CMOS) circuits and memristor crossbar arrays can execute neural network inference process with high energy efficiency [22]. Several

This article has been accepted for publication in a future issue of this journal, but has not been fully edited. Content may change prior to final publication. Citation information: DOI10.1109/JIOT.2024.3448350,

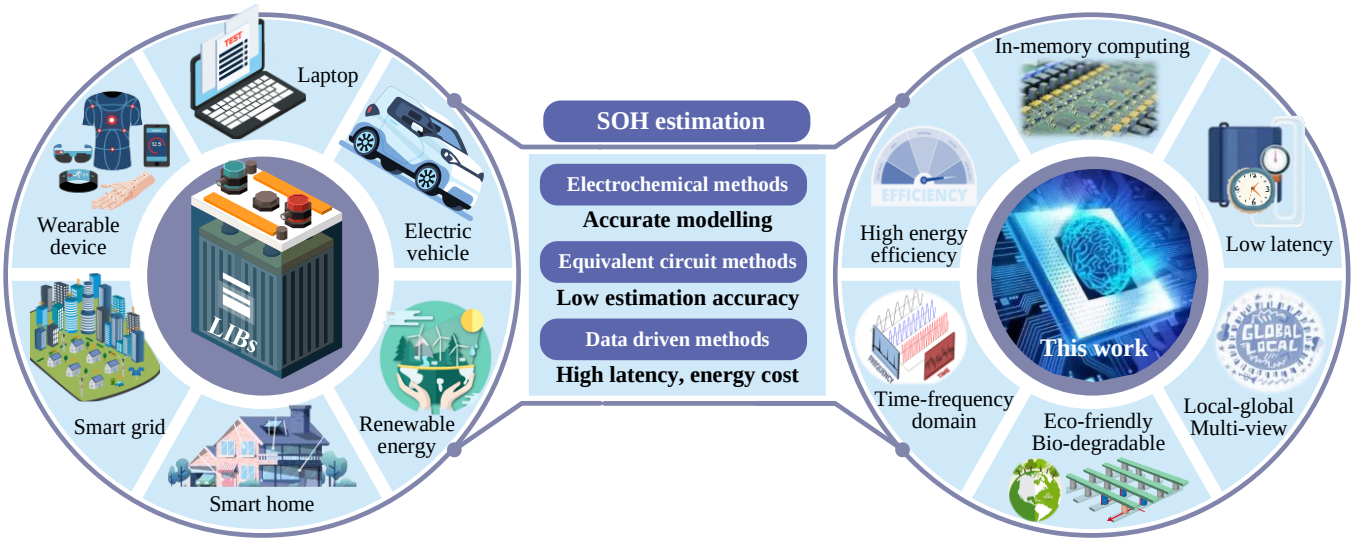

Fig. 1. Systemic comparison with the existing battery SOH estimation methods.

approaches have demonstrated that performing on-chip inference using memristor crossbar arrays achieves low energy consumption, low transmission latency, and high computing speeds [23-26]. However, realizing software-comparable computing accuracy with high energy efficiency and low latency remains challenging.

First, the existing neuromorphic computing systems almost based on metal-oxide memristors [21], highly stable and eco-friendly memristors and memristor crossbar arrays should be developed. Second, recent studies have focused on time-domain information processing, while frequency-domain information processing has rarely been considered. Third, research gaps exist regarding the development of time-frequency fusion strategies and local-global multiview learning mechanisms for neuromorphic computing architectures.

To leverage the potential of memristor-based neuromorphic computing in IoT scenarios, this work aims to investigate a time-frequency hybrid neuromorphic computing architecture for battery SOH estimation. For clarity, a systemic comparison with the existing battery SOH estimation methods is provided in Fig. 1. The primary contributions of this research are summarized as follows.

1) An emerging computing device, i.e., an eco-friendly, biodegradable memristor crossbar array, is constructed after the fabrication of a high-stability modified silk fibroin protein (MSFP)-based memristor, enabling high energy efficiency and high-performance density in the proposed system.

2) A circuit design is developed for the time-frequency feature fusion module, which can effectively fuse the time-frequency-domain information and provide comprehensive representations of perceptual information.

3) In contrast to the existing neuromorphic computing architectures, a time-frequency hybrid neuromorphic computing architecture is designed; this architecture can be perceived and processed from a local-global multiview perspective and demonstrates satisfactory performance (i.e., estimation accuracy, computing speed, and transmission latency) in battery SOH estimation tasks.

The remainder of this paper is organized as follows. Section II details the architecture of the proposed time-frequency hybrid neuromorphic computing system. Section III describes the process of preparing the MSFP-based memristor and the memristor crossbar array. Section IV elaborates on the detailed circuit design of the entire system, focusing on the local information extraction module, the time-frequency feature fusion module, and the global information perception module. Section V applies the proposed system to battery SOH estimation. Section VI concludes the paper with a summary of the research findings. Section VII discusses the future direction of this work.

II. Development of a Time-Frequency Hybrid Neuromorphic Computing Architecture

In this paper, we propose a time-frequency hybrid neuromorphic computing system that can efficiently extract local-global information in the time-frequency domain and provide reliable SOH estimates for lithium-ion batteries. To manage the complexity of the proposed time-frequency hybrid neuromorphic computing system, three modules are employed, i.e., a local information extraction module, a time-frequency feature fusion module, and a global information perception module, as shown in Fig. 2.

Local information extraction module: Based on the convolutional attention mechanism [27], a novel local information extraction module is designed to enhance the feature representation ability of the proposed approach. The local information extraction module is mainly composed of a 2-dimensional convolutional neural network (2D CNN) unit, a parallel multiscale (PM) self-attention unit, and a 1D convolution unit. Specifically, the electrical signals of lithium-ion batteries are denoted as $V_{i,j}$= {[$v_{i,j}$, $i_{i,j}$, $T_{i,j}$, $t_{i,j}$], i∈[1, n], j∈[1, m]}. $v_{i,j}$, $i_{i,j}$, $T_{i,j}$, and $t_{i,j}$ denote the voltage, current, temperature, and time, respectively. n is the number of lithium-ion batteries, and m is the number of discharge cycles.

This article has been accepted for publication in a future issue of this journal, but has not been fully edited. Content may change prior to final publication. Citation information: DOI10.1109/JIOT.2024.3448350,

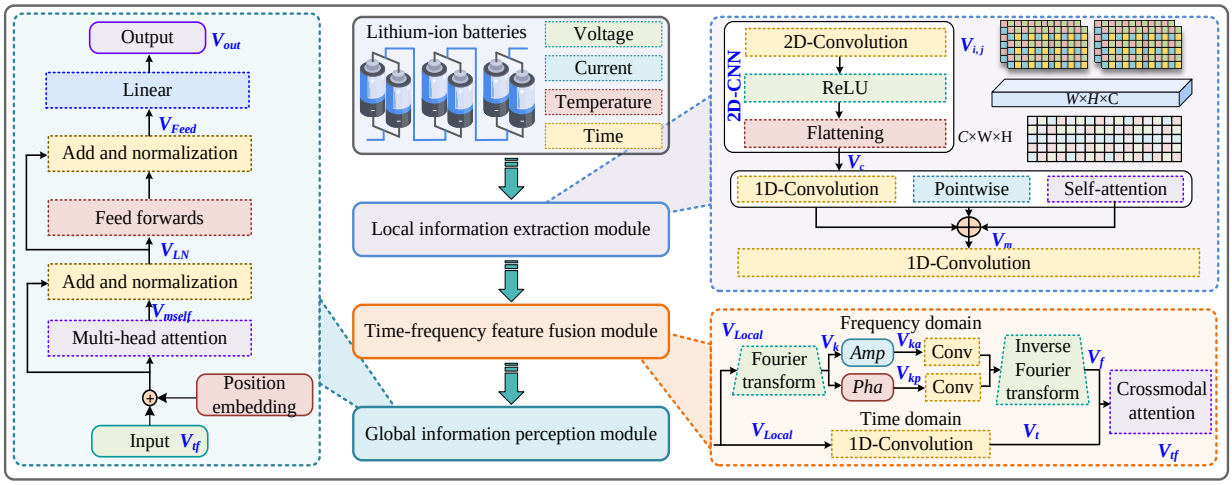

Fig. 2. Schematic of time-frequency hybrid neuromorphic computing system.

First, the 2D CNN unit is employed to capture detailed information from the electrical signals of lithium-ion batteries: V_c=2D-*conv* ($V_{i,j}$). Then, the PM self-attention unit is used to extract features with temporal dependencies, which can pay more attention to the useful information contained in electrical signals and suppress abrupt noise. The output of the PM self-attention unit is presented as V_m=PM self-attention (V_c). Furthermore, the obtained feature information V_m is delivered to the 1D convolution unit, which can smoothly filter the features and incorporate temporal dependencies. Thus, the local information representation can be represented by V_{Local}=1D-*conv* (V_m).

Time-frequency feature fusion module: The combination of time-domain information and frequency-domain information can provide more comprehensive representations of battery signals [28]. A time-frequency feature fusion module is designed in this work. First, the 1D convolution unit is used to process the time-domain information that can prevent overfitting problems and leave more space in the frequency domain: V_t=1D-*conv* (V_{Local}). Second, the fast discrete Fourier transform (DFT) operation is applied to extract the frequency-domain information from the input features V_k=DFT (V_{Local}). Third, parallel convolutional operations are performed on the amplitude V_{ka} and the phase V_{kp} of V_k. After the parallel convolutional operations, the fast inverse DFT (IDFT) operation is performed on the input signal, which can facilitate feature fusion from the time domain and frequency domain. The output of the fast IDFT operation can be represented as V_f= IDFT [1D-*conv* (V_{ka})+ 1D-*conv* (V_{kp})]. Furthermore, the cross-modal attention mechanism is employed, taking the frequency-domain features V_f as queries and the time-domain features V_t as keys and values, and the output of the time-frequency feature fusion module can be expressed as V_{tf}=cross-modal attention (V_t + V_f).

Global information perception module: Considering that the transformer network has advantages in terms of processing global information with long-range dependencies [29], we propose a global information perception module based on the transformer architecture. The output feature V_{tf} derived from the time-frequency feature fusion module is injected into the multi-head self-attention unit to generate global perception information: V_{mself}= multi-head self-attention (V_{tf}). Then, the output V_{out} of the global information perception module is obtained via residual connection, layer normalization, and linear operations.

To further improve the understanding of system design, the corresponding pseudocode is provided in Table I.

TABLE I
THE ALGORITHMIC PSEUDOCODE OF THE TIME-FREQUENCY HYBRID NEUROMORPHIC COMPUTING SYSTEM

Algorithm 1 Time-frequency hybrid neuromorphic computing system
Input: Electrical signals $V_{i,j}$= {[$v_{i,j}$, $i_{i,j}$, $T_{i,j}$, $t_{i,j}$], $i\in[1, n]$, $j\in[1, m]$}
Output: V_{out} representing the predicted capacity
procedure TFHNCS _ architecture ($V_{i,j}$)
Local information extraction module
for $i\in[1, n]$, $j\in[1, m]$ **do**
  $V_c\leftarrow$2D-*conv* ($V_{i,j}$)
  $V_m\leftarrow$PM self-attention (V_c)
  $V_{Local}\leftarrow$1D-*conv* (V_m)
end for
Time-frequency feature fusion module
$V_t\leftarrow$1D-*conv* (V_{Local})
$V_k\leftarrow$DFT (V_{Local})
$V_f\leftarrow$IDFT [1D-*conv* (V_{ka})+ 1D-*conv* (V_{kp})]
// V_{ka}, V_{kp} are amplitude and phase of V_k
$V_{tf}\leftarrow$cross-modal attention (V_t + V_f)
Global information perception module
$V_{mself}\leftarrow$multi-head self-attention (V_{tf})
$V_{LN}\leftarrow$layer normalization (V_{mself}, V_{tf})
$V_{Feed}\leftarrow$layer normalization (V_{LN}, ReLU ($W_a\cdot V_{LN}$)$\cdot W_b$)
// W_a, W_b are two linear transformation matrices
$V_{out}\leftarrow$linear (V_{Feed})
end procedure

III. MEMRISTOR TECHNOLOGY

To better understand the circuit design of the proposed time-frequency hybrid neuromorphic computing system, memristor technology is introduced in this part.

A. Memristor Fabrication and Characteristics

Silk fibroin protein (SFP), an excellent biomaterial that is environmentally sustainable and biodegradable, has shown great potential for use in brain-inspired computing [30]. In this work, an MSFP-based memristor is fabricated using the radio frequency (RF) magnetron sputtering method and the spin coating method. The former method is utilized to fabricate Au electrodes. The latter method is used to synthesize the MSFP

This article has been accepted for publication in a future issue of this journal, but has not been fully edited. Content may change prior to final publication. Citation information: DOI10.1109/JIOT.2024.3448350,

functional layer. The specific fabrication process (as shown in Fig. 3) is described below.

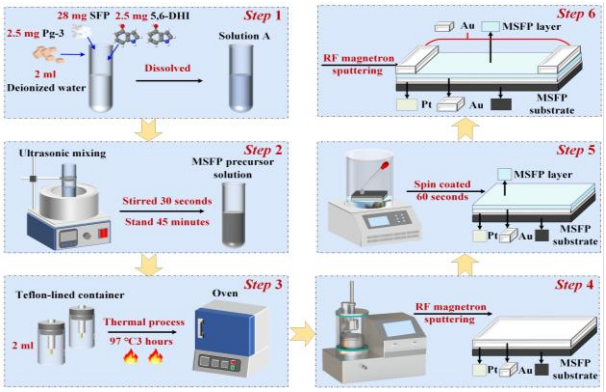

Fig. 3. Flow chart for preparing the Au/MSFP/Au memristor.

Step 1: 28 mg of freeze-dried SFP, 2.5 mg of polyglycerol-3 (Pg-3), and 2.5 mg of 5,6-dihydroxyindole (5,6-DHI) are dissolved in 2 mL of deionized water to prepare solution A.

Step 2: Solution A is continuously stirred using ultrasonic mixing for 30 seconds, and then an MSFP precursor solution with a black colour is obtained after performing statistical processing for 45 minutes.

Step 3: The MSFP precursor solution is transferred to an oven and then thermally processed at 97°C for 3 hours to fabricate the MSFP substrate.

Step 4: The RF magnetron sputtering method is used to fabricate the bottom Au electrode on the MSFP substrate under 0.8-Pa Ar and 15-W conditions for 35 seconds. Notably, a 5-nm Pt adhesion layer is prepared between the bottom Au electrode and the MSFP substrate.

Step 5: The MSFP precursor solution is spin coated on the bottom Au electrode using plasma treatment for 60 seconds to form the MSFP functional layer.

Step 6: The top Au electrode is synthesized on the MSFP functional layer using the RF magnetron sputtering method under 0.8-Pa Ar and 15-W conditions for 20 seconds. In this manner, the Au/MSFP/Au memristor is fabricated.

The electrical characterization of the fabricated Au/MSFP/Au memristor is carried out by using an electrochemical workstation (CHI-660D), as shown in Fig. 4.

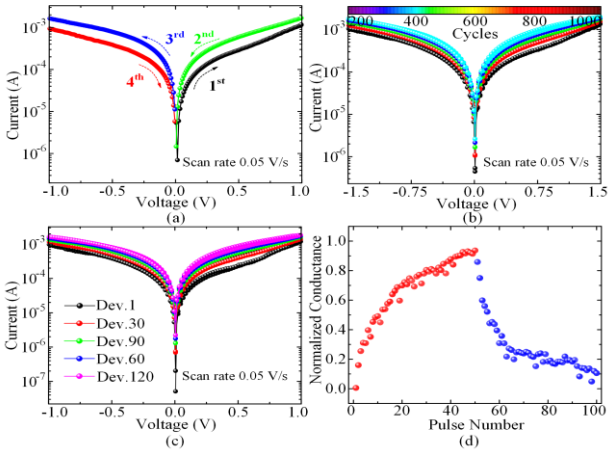

Fig. 4. (a) I-V curve of the Au/MSFP/Au memristor; (b) C2C stability of the Au/MSFP/Au memristor; (c) D2D stability of the Au/MSFP/Au memristor; (d) Normalized conductance.

The Au/MSFP/Au memristor exhibits typical analogue resistive switching behaviour under a continuous scanning voltage, and the scanning aptitude and scanning rate are set to 1V and 0.05V/s, respectively, as shown in Fig. 4(a). To study the cycle-to-cycle (C2C) stability of the Au/MSFP/Au memristor, more than 1000 I-V curves are measured on the same memristor. The typical analogue resistive switching behaviour can be effective maintained when the scanning voltage is increased to 1.5V, as shown in Fig. 4(b). Fig. 4(c) exhibits the extensive overlap I–V curves measured by the 120 randomly chosen memristors, and the Au/MSFP/Au memristor has good device-to-device (D2D) stability. The conductance of the Au/MSFP/Au memristor is measured under the voltage of 100 pulses, and the pulse aptitude and pulse width are fixed at 0.7V and 50μs, respectively, as shown in Fig. 4(d). Specifically, the conductance of the Au/MSFP/Au memristor increases when the voltage of 50 positive pulses is applied, exhibiting long-term potentiation (LTP) behaviour. When the voltage of 50 negative pulses voltage is applied, the conductance of the memristor gradually decreases, indicating long-term depression (LTD) behaviour.

B. Memristor-Based Crossbar Array

In this paper, a memristor-based crossbar array with a two-transistor-two-memristor (2T2M) configuration is designed, which can effectively realize negative and positive weights and parallel in-memory computing. The circuit architecture of the 2T2M crossbar array is shown in Fig. 5.

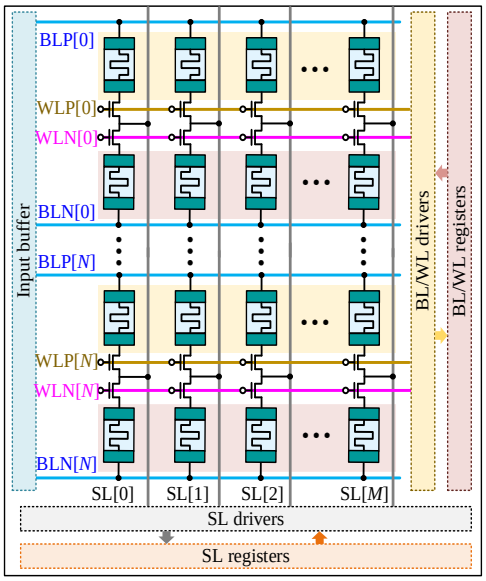

Fig. 5. Circuit architecture of the 2T2M crossbar array.

Compared with traditional memristor crossbar arrays with one-transistor-one-memristor (1T1M) configuration, each cell in the 2T2M crossbar array is connected to the same source lines (SLs), and subtraction can be performed directly in the current domain. The circuit design of the 2T2M crossbar array can greatly reduce the current passed through to the SL, which provides a potential remedy for avoiding IR issues. The Au/MSFP/Au memristors in the same row are controlled by word line (WL) signals and modulated depending on the SL

This article has been accepted for publication in a future issue of this journal, but has not been fully edited. Content may change prior to final publication. Citation information: DOI10.1109/JIOT.2024.3448350,

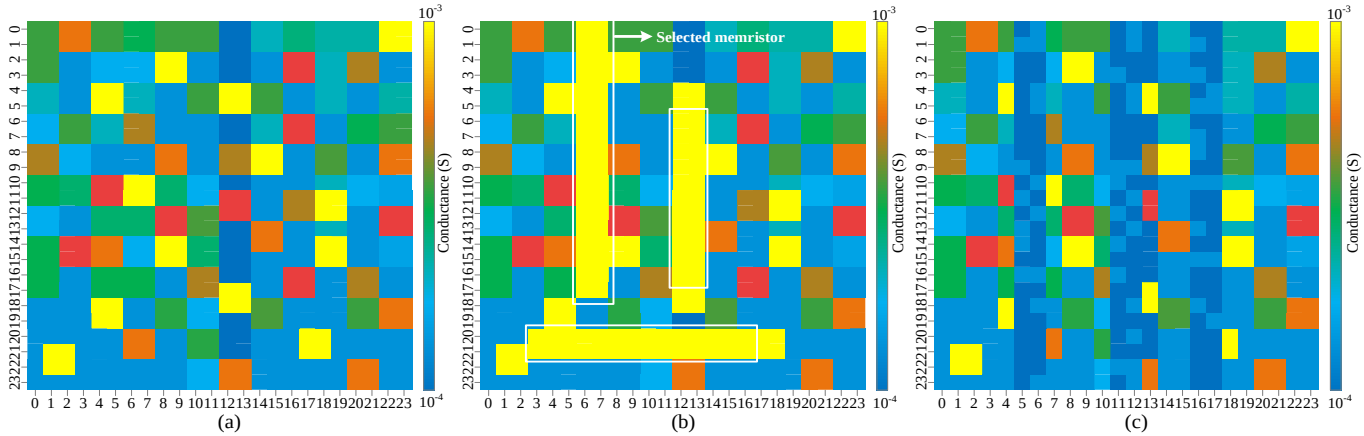

Fig. 6. Conductance programming ability of the proposed method. (a) Randomly programming; (b) Selected programming; (c) Column programming.

signals. The input voltages are applied to the bit lines (BLs), and the corresponding output voltage is read through the SLs.

To explore the conductance programming ability of the proposed method, a 24×24 2T2M crossbar array with 28-nm technology is selected. Fig. 6 shows the conductance response of the selected 2T2M crossbar array. First, the conductance of each memristor is randomly programmed to an intermediate value between the minimum conductance G_{on} and the maximum conductance G_{off}, as shown in Fig. 6(a). Then, the conductance of the selected memristors is programmed to the maximum conductance G_{off} using a pulse voltage with a pulse potential of 0.7V and a pulse width of 50μs, as shown in Fig. 6(b). Furthermore, the conductance of the 2T2M crossbar array with columns 5, 6, 11, 12, 16, and 17 selected is modulated to the minimum conductance G_{on} 50 after 50 voltage pulses, as shown in Fig. 6(c).

IV. Circuit Design of the Time–Frequency Hybrid Neuromorphic Computing System

Neuromorphic computing has given rise to next-generation computing diagrams for the implementation of energy-efficient hardware [31]. Our motivation is to construct a time-frequency hybrid neuromorphic computing system for battery SOH estimation, aiming at realizing low-power and high-density information processing in IoT scenarios.

A. Circuit Design of the Local Information Extraction Module

In this work, we propose a local information extraction module to increase the perception ability of the developed architecture and capture time-domain features $V_{Local}(t)$ with neighbourhood dependencies from electrical signals $V_{i,\,j}(t)$= $\{[v_{i,\,j},\ i_{i,\,j},\ T_{i,\,j},\ t_{i,\,j}],\ i\in[1,\ n],\ j\in[1,\ m]\}$. The specific circuit design of the local information extraction module is shown in Fig. 7.

First, each input derived from electrical signals $V_{i,\,j}(t)$ is converted to a k-channel feature voltage $V_c(t)$ by the 2D CNN unit. Here, 2D CNN mainly consists of a convolution unit and a flattening circuit. Second, the feature voltage $V_c(t)$ is injected into the PM self-attention unit, which is mainly composed of a pointwise transformation circuit, a convolution unit, and a self-attention circuit. Specifically, the pointwise transformation circuit is employed to capture the token feature $V_{pp}(t)$ from the input voltage $V_c(t)$ with linear operations. The convolution unit and the self-attention unit are used together, which enables the PM self-attention unit to be sensitive to both short-term and long-term structures. The output voltages of the convolution unit and the self-attention unit are denoted as $V_{cc}(t)$ and $V_{ss}(t)$, respectively. The output voltage $V_m(t)$ of the PM self-attention unit is the summation of the voltages of these three parallel units, which can be mathematically expressed as:

$$V_m(t) = V_{pp}(t) + V_{cc}(t) + V_{ss}(t) \tag{1}$$

$$V_{pp}(t) = \max\left(0, V_c(t)\cdot W_A\right)\cdot W_B \tag{2}$$

$$V_{cc}(t) = Conv\left(V_c(t)\right) \tag{3}$$

$$V_{ss}(t) = Attention\left(V_c(t)\right) \tag{4}$$

where W_A and W_B represent the weight matrices implemented by 2T2M crossbar arrays. $Conv(\cdot)$ and $Attention(\cdot)$ denote the convolution and self-attention operations, respectively.

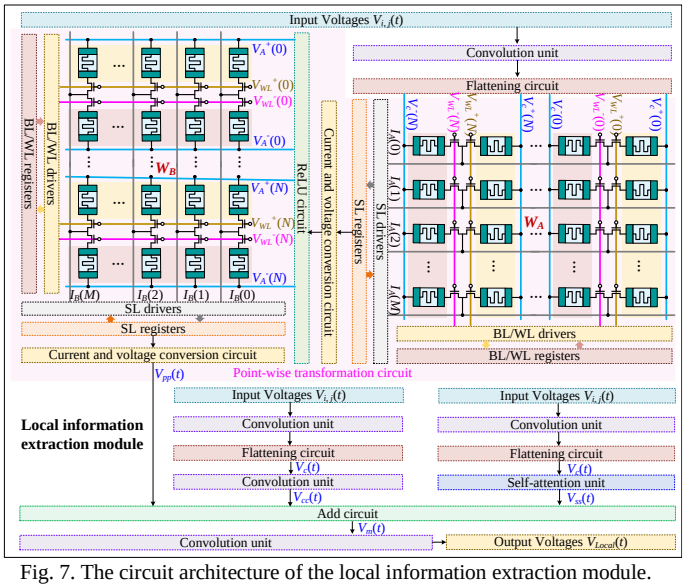

Fig. 7. The circuit architecture of the local information extraction module.

Furthermore, the voltage $V_m(t)$ is delivered to the convolution unit that can fuse time-domain dependencies and generate the final output $V_{Local}(t)$. The architectures of the flattening circuit and the rectified linear unit (ReLU) circuit were designed in previous work [32]. This work mainly focuses on the circuit designs of the convolution and self-attention units.

This article has been accepted for publication in a future issue of this journal, but has not been fully edited. Content may change prior to final publication. Citation information: DOI10.1109/JIOT.2024.3448350,

1) Circuit design of the convolution unit

The circuit design of the convolution unit, which consists of a 2T2M crossbar array, a current-to-voltage conversion circuit, and a ReLU circuit, is proposed and shown in Fig. 8.

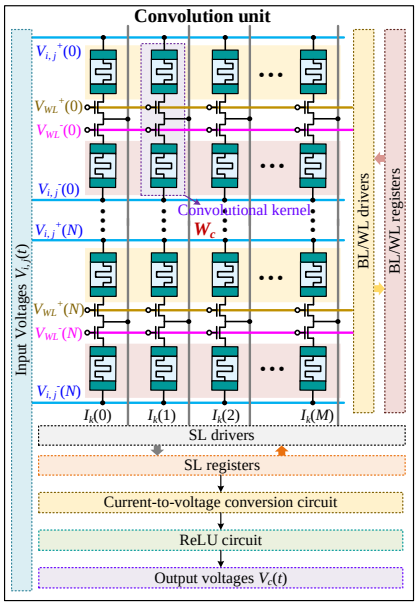

Fig. 8. Circuit design of the convolution unit.

In the convolution unit, the input signals $V_{i,j}(t)$ controlled by the BLs are injected into the 2T2M crossbar array in a row-by-row manner. To achieve high-efficiency convolution operations, the weights of the convolutional kernels are mapped to the conductance differences of the 2T2M crossbar arrays in this work. The convolution current $I_{k,j}(t)$ of the one-column 2T2M crossbar array is delivered to the current-to-voltage conversion circuit and ReLU circuit. Thus, the input and output of the convolution unit can be mathematically expressed by:

$$I_{k,j}(t) = \sum_{i=1}^{N} \left(G^{+}_{i,j} - G^{-}_{i,j} \right) \cdot V_{i,j}(t) \tag{5}$$

$$V_{c,j}(t) = \mathrm{Re}LU\left(convertor\left(I_{k,j}(t) \right) \right) \tag{6}$$

where $V_{c,j}(t)$ is the convolution voltage of the one-column 2T2M crossbar array and j denotes the dimensionality of the output voltage. $G^{+}_{i,j}$ and $G^{-}_{i,j}$ are the conductance levels of the top memristor and the bottom memristor, respectively. i and j denote the i_{th} row and j_{th} column of the 2T2M crossbar array, respectively. N and M represent the numbers of rows and columns in the 2T2M crossbar array, respectively. $ReLU(\cdot)$ and $convertor(\cdot)$ denote the ReLU and current-to-voltage conversion operations, respectively.

2) Circuit design of the self-attention unit

The self-attention unit is designed to enhance the ability to study key features and filter irrelevant information from the input signals. The self-attention unit is mainly composed of the 2T2M crossbar array, the current-to-voltage conversion circuit, the Hadamard product circuit, and the softmax circuit, as shown in Fig. 9.

In Fig. 9, the self-attention unit receives the input voltage $V_c(t)$ generated by the convolution unit. $\boldsymbol{W}$ (W_K, W_Q, W_V) are the weight matrixes to be learned, which are implemented by the 2T2M crossbar arrays. Following the learnable weight matrixes $\boldsymbol{W}$ (W_K, W_Q, W_V), the input voltages $V_c(t)$ can be converted to current vectors, denoting the attention key I_K, the attention query I_Q, and the attention value I_V, respectively. The output voltages $V_{ss}(t)$ of the self-attention unit can be obtained by applying the Hadamard product operation and softmax operation, which can be mathematically described as:

$$V_s = soft\max\left(\frac{convertor\left(W_K \cdot V_c \right)^T \cdot convertor\left(W_Q \cdot V_c \right)^T}{\sqrt{d_{ss}}} \right) \tag{8}$$

$$V_{ss} = V_s \cdot convertor\left(W_V \cdot V_c \right)^T \tag{9}$$

where d_{ss} and T represent the dimensionality of the self-attention unit and the transposition operation, respectively.

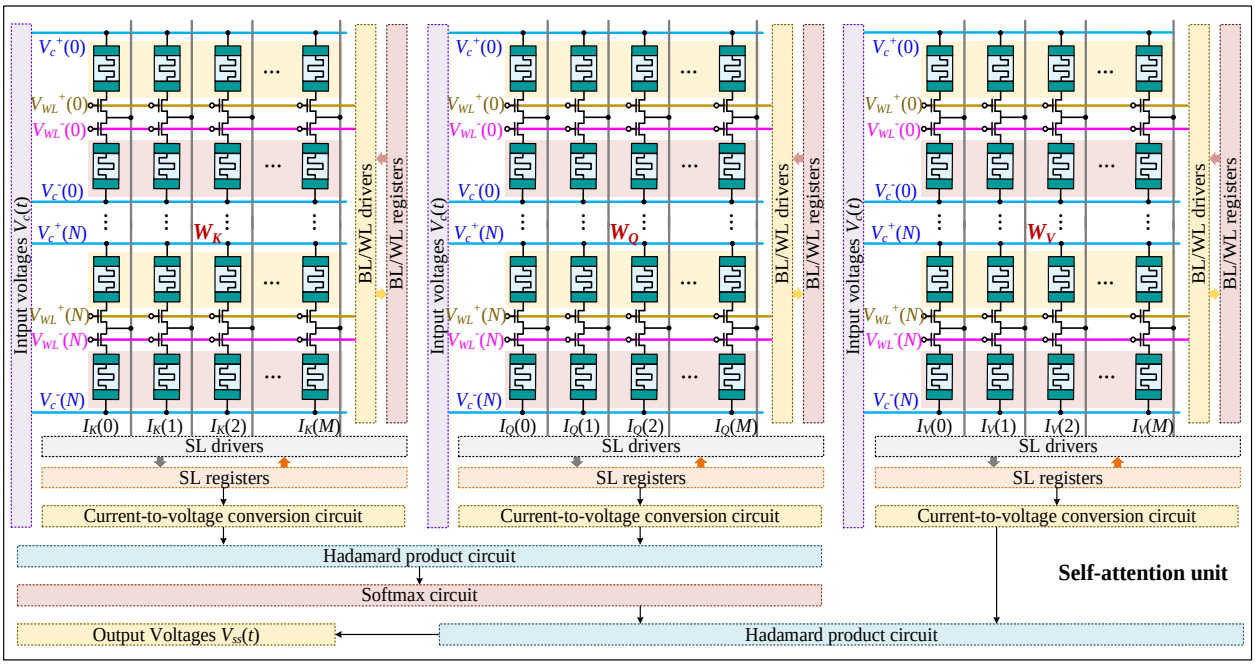

Fig. 9. Circuit design of the self-attention unit.

This article has been accepted for publication in a future issue of this journal, but has not been fully edited. Content may change prior to final publication. Citation information: DOI10.1109/JIOT.2024.3448350,

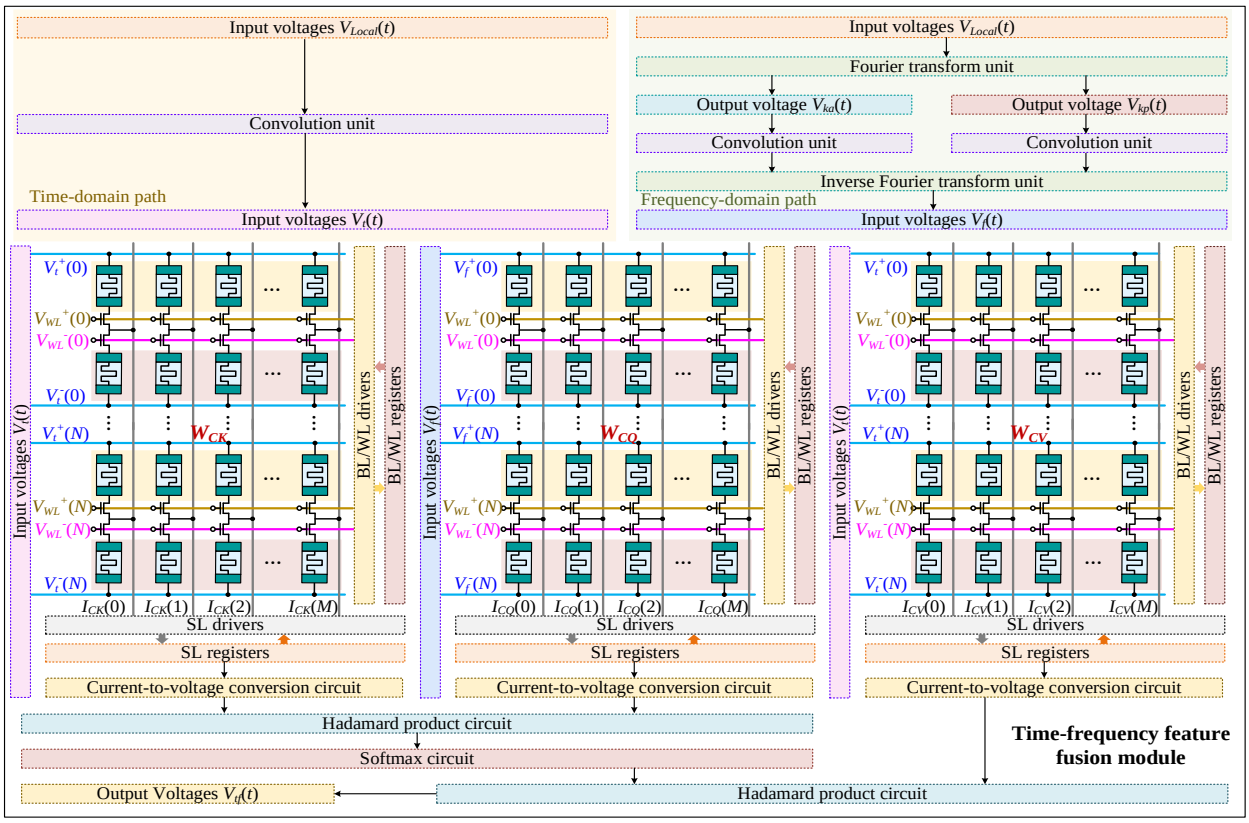

Fig. 10. Circuit design of the time-frequency feature fusion module.

$Softmax(\cdot)$ denotes the softmax operation, and $V_s(t)$ denotes the output voltage of the softmax circuit.

B. Circuit Design of the Time-Frequency Feature Fusion Module

In this work, we propose a time-frequency feature fusion module for capturing context information in the time domain and periodic information in the frequency domain, which can provide more comprehensive representations for the SOH estimation task. The specific circuit design of the time-frequency feature fusion module is shown in Fig. 10.

According to Fig. 10, the time-frequency feature fusion module includes two processing paths in the time domain and frequency domain. Along the time-domain path, the input signal $V_{Local}(t)$ is injected into the convolution unit, which can further extract time-domain features $V_t(t)$ and effectively avoid overfitting problems. Along the frequency-domain path, the Fourier transform unit is first applied to capture the corresponding frequency features (including the amplitude representation $V_{ka}(t)$ and the phase representation $V_{kp}(t)$) from the input signal $V_{Local}(t)$. Then, the amplitude representation $V_{ka}(t)$ and the phase representation $V_{kp}(t)$ are delivered to two convolution units. Furthermore, the inverse Fourier transform unit is employed to transfer the frequency-domain information to the time domain, which facilitates the subsequent time-frequency fusion process. Finally, a cross-modal attention unit receives the time-domain voltage $V_t(t)$ and the frequency-domain voltage $V_f(t)$. The 2T2M crossbar arrays are used to learn and calculate the weight matrices $\boldsymbol{W_c}$ (W_{CK}, W_{CQ}, W_{CV}) in the cross-modal attention unit. Following the weight matrices (W_{CK}, W_{CV}), the time-domain voltage $V_t(t)$ can be converted to current vectors, representing the attention key I_{CK} and the attention value I_{CV}, respectively. Following the weight matrix W_{CQ}, the frequency-domain voltage $V_f(t)$ can be transformed into an attention query I_{CQ}. After the Hadamard product operation and softmax operation are applied, the output voltages $V_{tf}(t)$ of the cross-modal attention unit can be obtained. The corresponding expression can be described as:

$$V_{tf} = V_{sc} \cdot convertor\left(W_{CV} \cdot V_t\right)^T \tag{10}$$

$$V_{sc} = soft\max\left(\frac{convertor\left(W_{CK} \cdot V_t\right)^T \cdot convertor\left(W_{CQ} \cdot V_f\right)^T}{\sqrt{d_{sc}}}\right) \tag{11}$$

where $V_{sc}(t)$ is the output voltage of the softmax circuit, and d_{sc} is the dimensionality of the cross-modal attention unit.

Notably, the circuit designs of the Fourier and inverse Fourier transform units are provided below.

According to [28], a complex sequence x_i can be converted into another complex sequence x_j with the same length via the DFT operation, which can be mathematically expressed as follows:

$$x_j = \frac{1}{\sqrt{P}} W_{DFT} \cdot x_i \tag{12}$$

where P is the number of points contained in the complex sequence x_i. W_{DFT} denotes the DFT matrix, it can be defined as:

$$W_{DFT} = \begin{bmatrix} 1 & 1 & \cdots & 1 \\ 1 & \omega & \cdots & \omega^{P-1} \\ \cdots & \cdots & \cdots & \cdots \\ 1 & \omega^{P-1} & \cdots & \omega^{(P-1)(P-1)} \end{bmatrix}, \omega = e^{-2\pi i/P} \tag{13}$$

This article has been accepted for publication in a future issue of this journal, but has not been fully edited. Content may change prior to final publication. Citation information: DOI10.1109/JIOT.2024.3448350,

In this paper, the Fourier and inverse Fourier transform units are designed by combining four same-size 2T2M crossbar arrays into integrated DFT and IDFT matrices, which can directly produce the real and imaginary parts of the DFT and IDFT outputs in a single operation. The Fourier and inverse Fourier transform units mainly consist of the 2T2M crossbar array, the current-to-voltage converter, and the analogue-to-digital converter (ADC), as illustrated in Fig. 11.

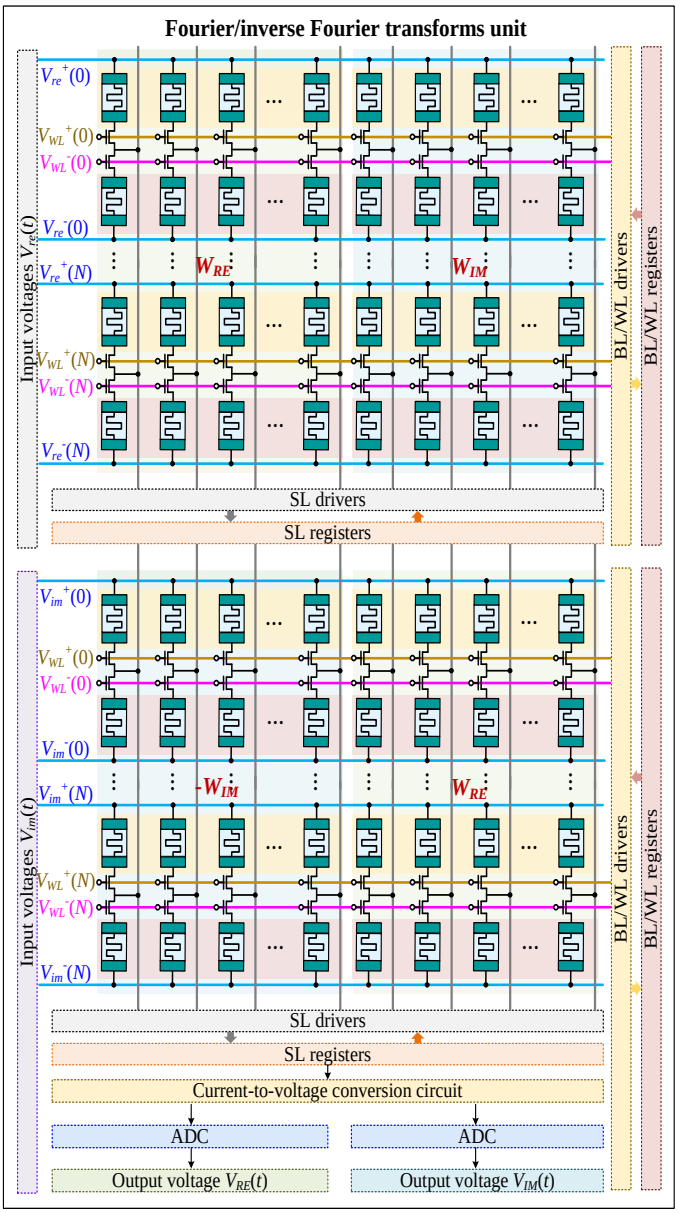

Fig. 11. Circuit design for the Fourier and inverse Fourier transform units.

According to Fig. 11, the DFT matrix W_{DFT} is mapped on the 2T2M crossbar array as conductance information, and the input complex sequence x_i is denoted as the input voltage:

$$\begin{bmatrix} V_{RE} \\ V_{IM} \end{bmatrix} = convertor\left\{ \frac{1}{\sqrt{P}} \begin{bmatrix} W_{RE} & -W_{IM} \\ W_{IM} & W_{RE} \end{bmatrix} \cdot \begin{bmatrix} V_{re} \\ V_{im} \end{bmatrix} \right\} \quad (14)$$

where W_{RE} and W_{IM} are the real and imaginary parts of the DFT matrix W_{DFT}, respectively, which are implemented by a 2T2M crossbar array. Similarly, the input/output voltages of the Fourier transform unit can be decomposed into real parts $V_{re}(t)$ and $V_{RE}(t)$ and imaginary parts $V_{im}(t)$ and $V_{IM}(t)$.

The IDFT operation can be implemented on the same circuit architecture as shown in Fig. 11. The input/output voltages of the inverse Fourier transform unit can be denoted as:

$$\begin{bmatrix} V_{re} \\ V_{im} \end{bmatrix} = convertor\left\{ \sqrt{p} \begin{bmatrix} W_{RE} & W_{IM} \\ -W_{IM} & W_{RE} \end{bmatrix} \cdot \begin{bmatrix} V_{RE} \\ V_{IM} \end{bmatrix} \right\} \quad (15)$$

C. Circuit Design of the Global Information Perception Module

In this work, a global information perception module based on a transformer mechanism is designed to learn global information with long-range dependencies regardless their time-domain distances. The specific circuit design of the global information perception module is shown in Fig. 12.

According to Fig. 12, the global information perception module mainly consists of a multi-head self-attention unit, a feedforward unit, and a linear circuit. First, the multi-head self-attention unit is fed the input voltage $V_{tf}(t)$ generated by the time-frequency feature fusion module. Then, the input voltage $V_{tf}(t)$ is projected and processed by three trainable weight matrices $\boldsymbol{W^n}$ (W^n_K, W^n_Q, W^n_V) that are implemented by 2T2M crossbar arrays. Subsequently, the input voltages $V_{tf}(t)$ can be transferred to current vectors, which denote as the multi-head attention key I^n_K, the multi-head attention query I^n_Q, and the multi-head attention value I^n_V, respectively. By implementing the Hadamard product and softmax operations, the voltage vectors, representing the learnable attention scores, can be obtained and described as follows:

$$V_{sg} = soft\max\left(\frac{convertor\left(W^n_K \cdot V_{tf}\right)^T \cdot convertor\left(W^n_Q \cdot V_{tf}\right)^T}{\sqrt{d_{sg}}} \right) \quad (16)$$

$$V_{mself} = V_{sg} \cdot convertor\left(W^n_V \cdot V_{tf}\right)^T \quad (17)$$

where $V_{sg}(t)$ and $V_{mself}(t)$ are the output voltages of the softmax circuit and multi-head self-attention unit, respectively. d_{sg} is the dimensionality of the multi-head self-attention unit.

Then, the feedforward circuit is used to process the output voltage $V_{mself}(t)$ of the multi-head attention unit, which is composed of two linear transformation matrices (W_a, W_b) implemented by 2T2M crossbar arrays, a ReLU circuit, and a layer normalization circuit. The output voltage $V_{Feed}(t)$ of the feedforward circuit is represented by:

$$V_{LN} = LN\left(V_{mself}, V_{tf}\right) \quad (18)$$

$$V_{Feed} = LN\left(V_{LN}, \mathrm{Re}LU\left(W_a \cdot V_{LN}\right) \cdot W_b\right) \quad (19)$$

where $V_{LN}(t)$ is the output voltage of the first layer normalization circuit. $LN(\cdot)$ denotes the layer normalization operation.

In the end, the final output of the global information perception module is obtained from the linear circuit, which is represented by:

$$V_{out} = Linear\left(V_{Feed}\right) \quad (20)$$

where $Linear(\cdot)$ represents a linear operation.

This article has been accepted for publication in a future issue of this journal, but has not been fully edited. Content may change prior to final publication. Citation information: DOI10.1109/JIOT.2024.3448350,

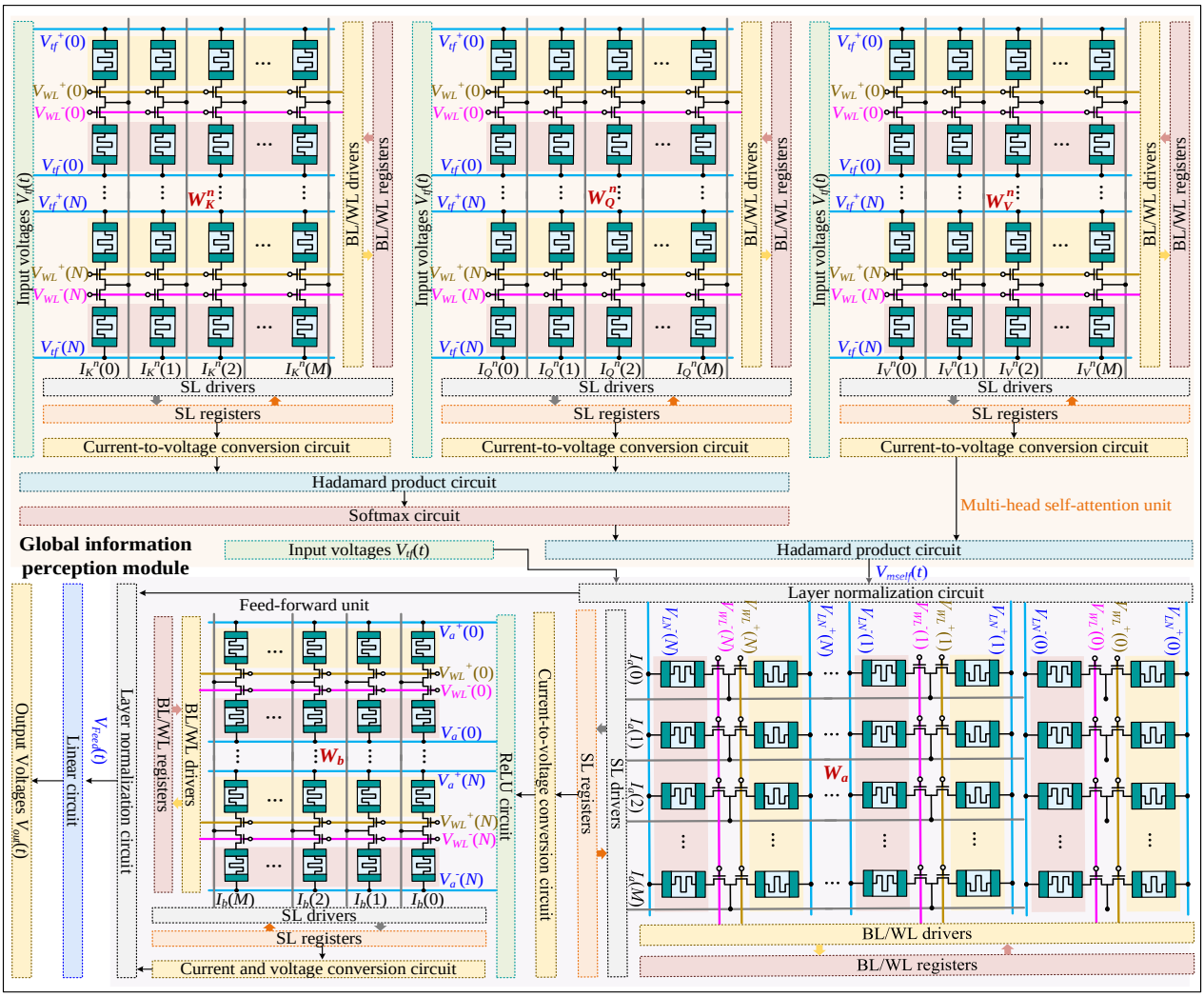

Fig. 12. Circuit design of the global information perception module.

V. Battery SOH Estimation Application

To validate the effectiveness and advantages of the proposed time-frequency hybrid neuromorphic computing system in battery SOH estimation, a series of experiments are conducted by using the necessary parameters (including circuit parameters and neural network parameters), as illustrated in Table II.

TABLE II
List of the parameters used for the time-frequency hybrid neuromorphic computing system

	Device	Parameter	
Circuit parameters	2T2M memristor crossbar array	R_{on}	1kΩ
		R_{off}	10kΩ
		V_{read}	0.7V
		V_{scan}	0.05V/s
		V_{WL}	1.0V
		V_{BL}	1.0V
		V_{min}	0V
		V_{max}	2.0V
	Transistor	V_{Gate}	1.1V
		R_{access}	15KΩ
	ADC	Precision	6bits
Neural network parameters		Learning rate	1.5×10^{-4}
		Batch size	10
		Momentum	0
		Decay	0.9
		Maximum error	10^{-4}

A. Dataset Description and Evaluation Metrics

Two publicly available battery ageing datasets are employed in this paper: the CS2 dataset collected by the computer-aided life cycle engineering center (CALCE) [33] and the NASA dataset released by the National Aeronautics and Space Administration (NASA) [34].

From the CALCE-CS2 dataset, four $LiCoO_2$ batteries (CS2_35, CS2_36, CS2_37, and CS2_38), each with an initial capacity of 1100 mAh, are used. The batteries are charged at a constant current (CC) of 0.5 C until the cut-off voltage reaches 4.2 V, and then the batteries are charged at a constant voltage (CV) of 4.2 V until the charging current decreases to 50 mA. After fully charging, the batteries are discharged at a constant current of 1 C until the cut-off voltage decreases to 2.7 V. Notably, the CALCE-CS2 dataset was obtained by a battery experimental test system (ArbinBT2000) under ambient conditions (25°C~30°C).

From the NASA dataset, four groups of $LiCoO_2$ lithium-ion batteries with initial capacities of 2000 mAh are selected: B05, B06, B07, and B18. The NASA dataset was obtained under charging and discharging conditions and measured by electrochemical impedance spectroscopy (EIS) at room temperature (24°C). Under charging conditions, a constant

This article has been accepted for publication in a future issue of this journal, but has not been fully edited. Content may change prior to final publication. Citation information: DOI10.1109/JIOT.2024.3448350,

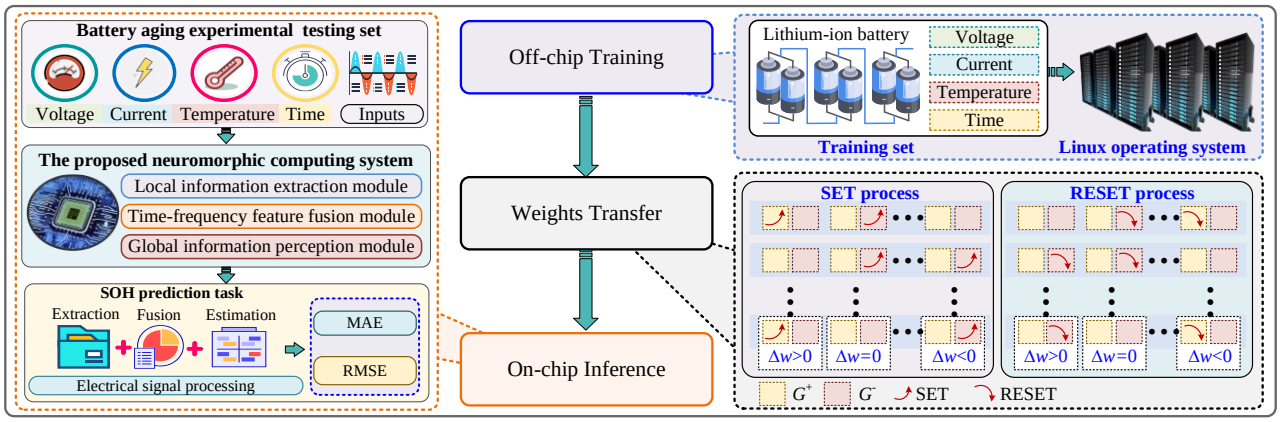

Fig. 13. Flow chart of neural network and inference processes.

current of 0.75 C is employed to charge the batteries until the cut-off voltage reaches 4.2 V, and then the batteries are charged at a constant voltage of 4.2 V until the current drops to 20 mA. Under discharging conditions, a constant current of 1 C is employed to discharge the batteries until the cut-off voltages of B05, B06, B07, and B18 decrease to 2.7 V, 2.5 V, 2.2 V, and 2.5 V, respectively. More detailed information about the two publicly available battery ageing datasets is shown in Table III.

TABLE III
DETAILED INFORMATION ABOUT THE TWO PUBLICLY AVAILABLE BATTERY AGEING DATASETS

Dataset	CALCE-CS2	NASA
Manufacturer	Unknown	LG Chem
Form factor	Prismatic	18650
Cell node	Graphite	Graphite
Cell cathode	$LiCoO_2$	$LiCoO_2$
Charging condition	CC-CV	CC-CV
Discharging condition	1 C	1 C
Nominal capacity	1100 mAh	2000 mAh
Upper cut-off voltage	4.2 V	4.2 V
Lower cut-off voltage	2.7 V	2.7 V, 2.5 V, 2.2 V, 2.5 V
Number of cells	4	4

To objectively evaluate the performance of the proposed time-frequency hybrid neuromorphic computing system, two evaluation metrics, namely, the mean absolute error (MAE) and root mean square error (RMSE), are used [35]. Notably, smaller MAE and RMSE values indicate higher estimation accuracy. The abovementioned evaluation metrics can be mathematically expressed as follows:

$$MAE = \frac{1}{n}\sum_{i=1}^{n}\left|C_i^{real} - C_i^{predicted}\right| \tag{21}$$

$$RMSE = \sqrt{\frac{1}{n}\sum_{i=1}^{n}\left(C_i^{real} - C_i^{predicted}\right)^2} \tag{22}$$

where C_i^{real} and $C_i^{predicted}$ denote the real battery capacity and the predicted battery capacity, respectively.

B. Neural Network Training and Inference Processes

The proposed time-frequency hybrid neuromorphic computing system is trained to perform the battery SOH estimation task, which mainly consists of an off-chip training stage, a weight transfer stage, and an on-chip inference stage, as illustrated in Fig. 13.

Off-chip training stage: The off-chip training process is implemented in Python with the PyTorch library and validated on a Linux operating system (Intel® Xeon(R) Gold 6242R CPU @ 3.10GHz CPU, Nvidia RTX 3090 GPU). Notably, the electrical signals in the CACLE-CS2 dataset are divided into a training dataset and a testing dataset based on a three-to-one ratio. For example, when the electrical signals in the CS2_35 cell are selected as the testing dataset, the remaining battery data for the other three cells are used as the training dataset. For the NASA dataset, the first 70% of the discharge cycles are distributed to the training dataset, and the remaining cycles are selected as the testing dataset. Gaussian random noise is injected during the off-chip training process to enhance the resilience of the proposed system against nonidealities in the SOH estimation task. The desired weights can be achieved when the off-chip training procedure is completed.

Weight transfer stage: The desired weights of the well-trained model are transferred to the proposed time-frequency hybrid neuromorphic computing system as the conductance levels using the cycle-parallel conductance tuning method [36]. Specifically, if the weight update direction is negative ($\Delta w<0$), a SET pulse is applied to the negative memristor cell (G^-) to decrease its weight; if the weight update direction is positive ($\Delta w>0$), a SET pulse is applied to the positive memristor cell (G^+) to increase its weight. In the RESET operation, a RESET pulse is applied to the corresponding memristor cell via the same procedure as that used by the SET operation. Notably, the RESET and SET operations are employed alternately for 2T2M crossbar array programming.

On-chip learning stage: The on-chip inference process is implemented in the NeuroSim V3.0 framework [37]. After the desired weights are transferred to the 2T2M crossbar array, the proposed time-frequency hybrid neuromorphic computing system is validated on the testing dataset using on-chip inference. When the electrical signals in the testing set are injected into the BLs of each crossbar array, the output of the global information perception module (representing the predicted battery capacity) can be obtained.

C. Results and Analysis

In this paper, a well-trained time-frequency hybrid neuromorphic computing system is employed to perform SOH estimation. The circuit results of the proposed time-frequency hybrid neuromorphic computing system are illustrated in Fig. 14 and Fig. 15.

This article has been accepted for publication in a future issue of this journal, but has not been fully edited. Content may change prior to final publication. Citation information: DOI10.1109/JIOT.2024.3448350,

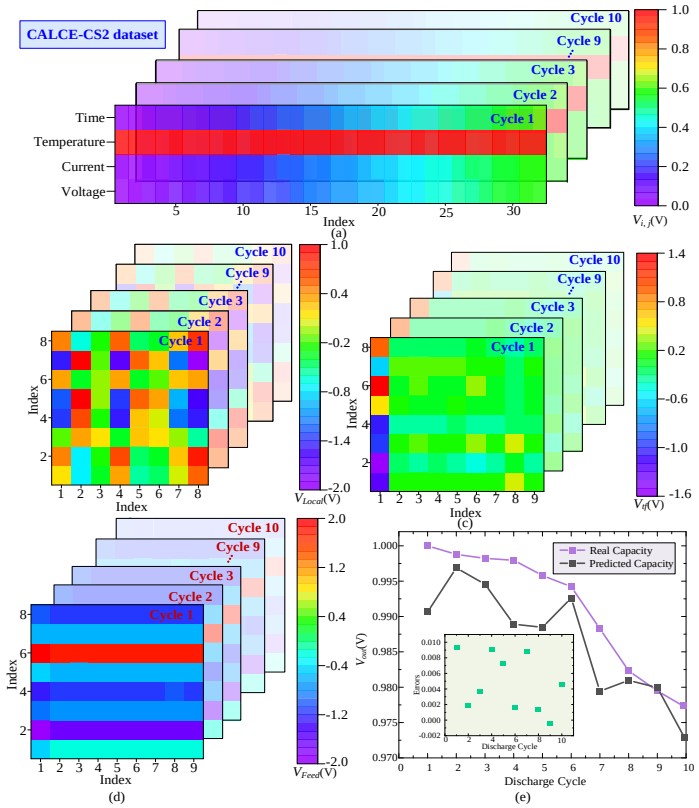

Fig. 14. Circuit results obtained by the proposed system on the CS2_35 cell. (a) Input signals; (b) The output voltage of the local information extraction module; (c) The output voltage of the time-frequency feature fusion module; (d) The output voltage of the feedforward circuit; (e) The output voltage of the global information perception module.

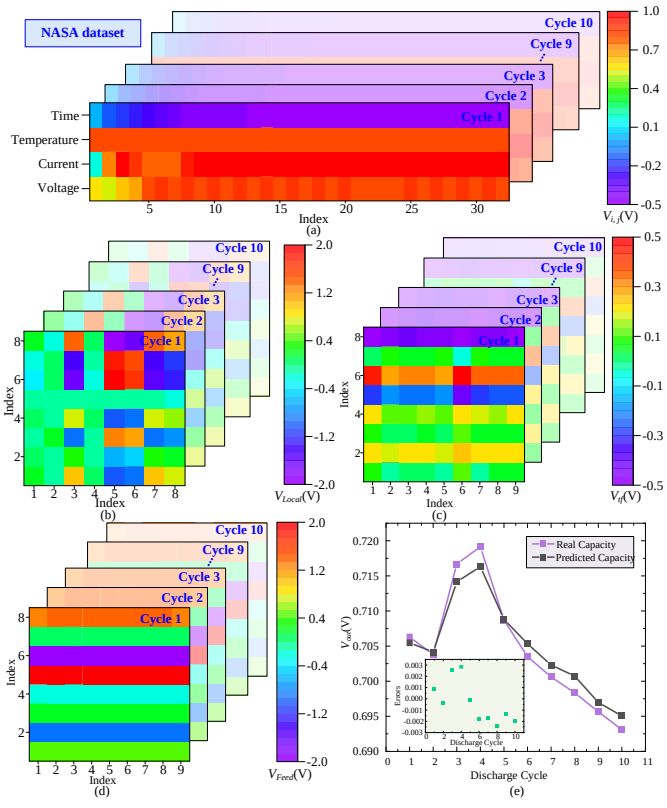

Fig. 15. Circuit results obtained by the proposed system on the B05 cell. (a) Input signals; (b) The output voltage of the local information extraction module; (c) The output voltage of the time-frequency feature fusion module; (d) The output voltage of the feedforward circuit; (e) The output voltage of the global information perception module.

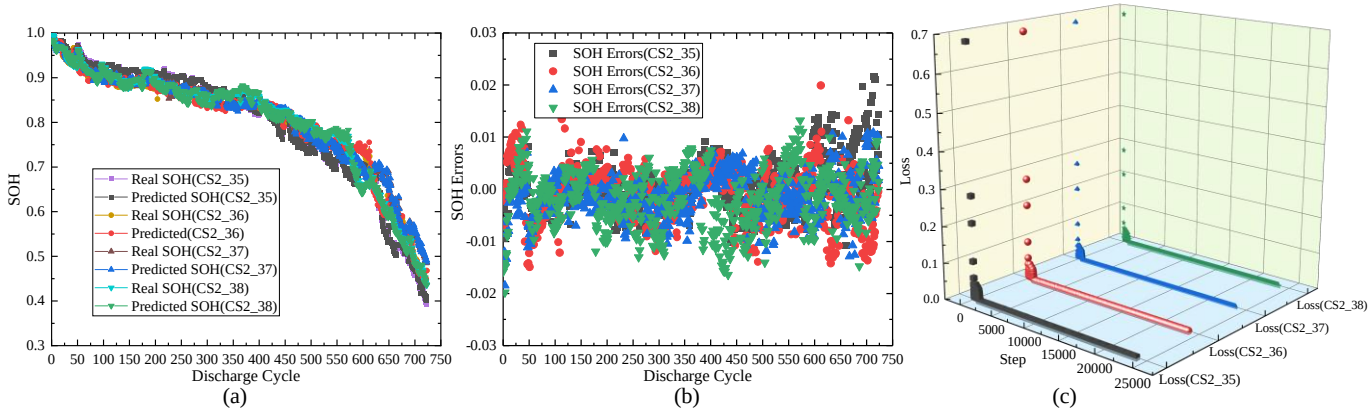

Fig. 16. Performance of the proposed system on the CALCE-CS2 dataset. (a) SOH estimation results; (b) SOH estimation errors; (c)training loss.

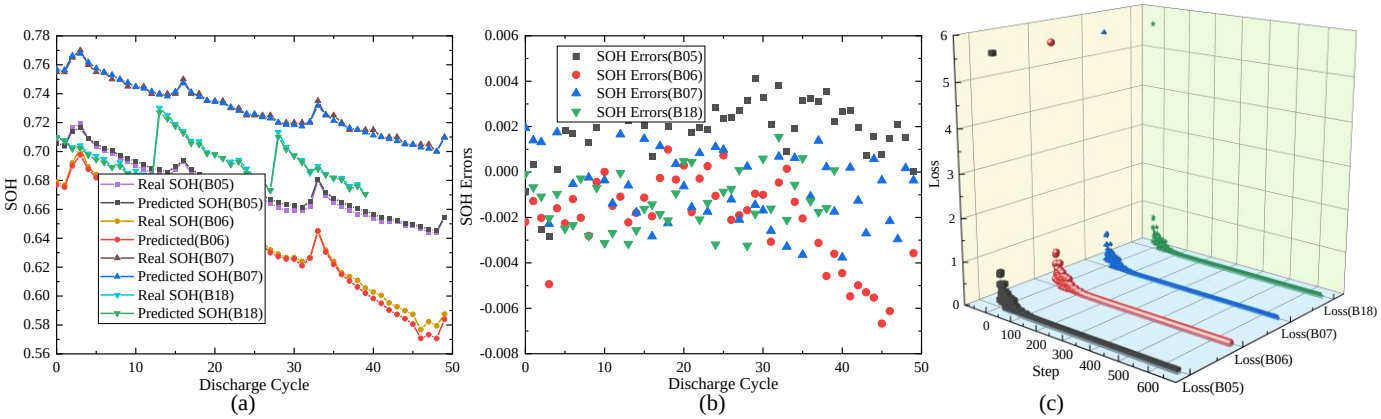

Fig. 17. Performance of the proposed system on the NASA dataset. (a) SOH estimation results; (b) SOH estimation errors; (c)training loss.

This article has been accepted for publication in a future issue of this journal, but has not been fully edited. Content may change prior to final publication. Citation information: DOI10.1109/JIOT.2024.3448350,

Specifically, the electrical signals (including voltage, current, temperature, and time signals) derived from two publicly available battery ageing datasets can be converted and reshaped to voltage maps $V_{i,j}(t)$ within the range of [0V, 1V]. These voltage maps are enrolled and injected into the proposed time-frequency hybrid neuromorphic computing system. The inputs and outputs of three modules, i.e., the local information extraction module, time-frequency feature fusion module, and global information perception module, are illustrated in Fig. 14 and Fig. 15. The final output voltage $V_{out}(t)$ represents the predicted capacity of the tested lithium-ion batteries, which can be used to calculate the SOH (the ratio of the remaining lithium-ion battery capacity to the original capacity) and is mathematically expressed by:

$$SOH = \frac{C_{current}}{C_{original}} \tag{23}$$

where $C_{current}$ and $C_{original}$ denote the current battery capacity and the original battery capacity, respectively.

To measure the estimation performance of the proposed time-frequency hybrid neuromorphic computing system, an experiment is conducted for 750 discharge cycles on CACLE-CS2 dataset. Meanwhile, another experiment is conducted for 50 discharge cycles on NASA dataset. To observe the performance of the proposed system, the SOH estimation results, errors, and training loss obtained on the CALCE-CS2 dataset and the NASA dataset are shown in Fig. 16 and Fig. 17, respectively. From Fig. 16 and Fig. 17, slight divergences are observed between the predicted SOHs and the real SOHs for the CALCE-CS2 dataset and the NASA dataset, demonstrating that the proposed system is capable of estimating battery SOH trends.

To verify the superiority of the proposed time-frequency hybrid neuromorphic computing system, experiments comparing it with the state-of-the-art (SOTA) estimation methods [12-20] are further conducted on the CALCE-CS2 dataset and the NASA dataset, as shown in Table IV and Table V, respectively. The proposed time-frequency hybrid neuromorphic computing system achieves the best estimation accuracy across four $LiCoO_2$ batteries (CS2_35, CS2_36, CS2_37, and CS2_38) on the CALCE-CS2 dataset. The proposed system exhibits a 0.15% average MAE decrease and a 0.19% average RMSE decline over the other methods. In the case of the NASA dataset, the proposed system still obtains the best accuracy for the SOH estimation task across the four groups of $LiCoO_2$ lithium-ion batteries (B05, B06, B07, and B18). The average values are greater than those of the SOTA methods, where the average MAE is decreased by 0.15% and the average RMSE is declined by 0.22%.

To investigate the effectiveness of each module in the proposed time-frequency hybrid neuromorphic computing system, a series of ablation experiments are conducted on the two publicly available battery ageing datasets. Two evaluation metrics, i.e., the MAE and RMSE, are collected in Table VI and Table VII, respectively.

From Table VI and Table VII, the results of the ablation experiments can be summarized as follows. 1) By comparing the estimation results, a discernible decline in estimation performance (CALCE-CS2 dataset: −0.21% MAE and −0.23% RMSE; NASA dataset: −0.17% MAE and −0.20%) can be

TABLE IV
COMPARISON OF DIFFERENT STATE-OF-THE-ART METHODS FOR SOH ESTIMATION ON CALCE-CS2 DATASET

Method	CALCE-CS2 dataset									
	CS2_35		CS2_36		CS2_37		CS2_38		Average	
	MAE	RMSE	MAE	RMSE	MAE	RMSE	MAE	RMSE	MAE	RMSE
[12]	1.55%	2.46%	1.16%	2.10%	1.16%	2.08%	1.74%	3.08%	1.40%	2.47%
[13]	0.68%	0.79%	0.81%	0.89%	0.75%	0.84%	0.68%	0.78%	0.73%	0.82%
[14]	0.77%	1.58%	1.56%	3.99%	0.93%	1.71%	0.78%	1.64%	1.01%	2.45%
[15]	0.25%	0.35%	0.47%	0.55%	0.37%	0.48%	0.39%	0.50%	0.37%	0.47%
[16]	0.43%	/	0.48%	/	0.42%	/	0.43%	/	0.44%	/
[17]	0.51%	0.65%	0.47%	0.64%	0.50%	0.69%	0.51%	0.66%	0.50%	0.66%
[18]	0.35%	0.45%	0.38%	0.48%	0.32%	0.42%	0.35%	0.43%	0.35%	0.45%
[19]	0.47%	1.32%	0.68%	2.01%	0.46%	1.10%	0.55%	1.34%	0.54%	1.48%
This work	0.18%	0.24%	0.22%	0.27%	0.17%	0.23%	0.23%	0.28%	0.20%	0.26%

Note: Best results are highlighted as first and second.

TABLE V
COMPARISON OF DIFFERENT STATE-OF-THE-ART METHODS FOR SOH ESTIMATION ON NASA DATASET

Method	NASA dataset									
	B05		B06		B07		B18		Average	
	MAE	RMSE	MAE	RMSE	MAE	RMSE	MAE	RMSE	MAE	RMSE
[12]	1.78%	2.15%	1.82%	2.10%	0.54%	0.67%	1.90%	2.08%	1.51%	1.75%
[13]	2.53%	2.71%	0.74%	0.88%	0.74%	0.97%	0.56%	0.71%	1.18%	1.58%
[14]	1.89%	1.52%	1.74%	1.78%	1.77%	1.63%	1.88%	1.92%	1.82%	1.71%
[15]	0.31%	0.42%	0.40%	0.51%	0.39%	0.40%	0.43%	0.54%	0.36%	0.46%
[16]	0.62%	/	1.05%	/	0.59%	/	1.02%	/	0.82%	/
[17]	0.27%	0.32%	0.74%	1.11%	0.17%	0.23%	0.25%	0.35%	0.36%	0.50%
[18]	0.53%	0.60%	0.49%	0.60%	0.41%	0.50%	0.41%	0.45%	0.46%	0.54%
[20]	0.28%	0.37%	0.44%	0.56%	0.37%	0.44%	0.42%	0.53%	0.36%	0.45%
This work	0.22%	0.24%	0.25%	0.33%	0.15%	0.18 %	0.15%	0.18%	0.19%	0.23%

Note: Best results are highlighted as first and second.

This article has been accepted for publication in a future issue of this journal, but has not been fully edited. Content may change prior to final publication. Citation information: DOI10.1109/JIOT.2024.3448350,

TABLE VI
ABLATION EXPERIMENTS ON CALCE-CS2 DATASET

Local information extraction module	Time-frequency feature fusion module			Global information perception module	Metrics	
PM-self-attention	Time-domain	Frequency domain	Fusion		MAE	RMSE
×	✓	✓	✓	✓	0.41%	0.49%
✓	×	✓	✓	✓	0.33%	0.40%
✓	✓	×	✓	✓	0.28%	0.37%
✓	✓	✓	×	✓	0.34%	0.42%
✓	✓	✓	✓	×	0.27%	0.36%
✓	✓	✓	✓	✓	0.20%	0.26%

TABLE VII
ABLATION EXPERIMENTS ON NASA DATASET

Local information extraction module	Time-frequency feature fusion module			Global information perception module	Metrics	
PM-self-attention	Time-domain	Frequency domain	Fusion		MAE	RMSE
×	✓	✓	✓	✓	0.36%	0.43%
✓	×	✓	✓	✓	0.36%	0.47%
✓	✓	×	✓	✓	0.30%	0.41%
✓	✓	✓	×	✓	0.31%	0.40%
✓	✓	✓	✓	×	0.25%	0.34%
✓	✓	✓	✓	✓	0.19%	0.23%

observed when the PM self-attention unit is removed from the local information extraction module. The main reason for this finding may be that the PM self-attention unit is able to guide the proposed system to capture features with temporal dependencies, effectively suppressing abrupt noise. 2) Compared with the frequency domain, the removal of the time domain from the time-frequency feature fusion module has a greater impact on the resulting estimation performance. Meanwhile, when the time domain features are used together with the frequency domain features, the estimation performance is slightly better than using a single domain feature. The main reasons can be concluded that the time-domain features play an important role in battery estimation, and the frequency-domain features can provide additional representations for the time domain. 3) There is a significant drop in estimation performance on the these two datasets (i.e., the CALCE-CS2 dataset and the NASA dataset), when the global information perception module is removed. The experimental results demonstrated that the global information perception module based on a transformer mechanism play the critical role in learning global information with long-range dependencies.

D. Computational Efficiency Analysis

Almost all the neuromorphic computing systems perform the on-chip inference with high energy efficiency using memristor crossbar arrays although using software operating system to implement the off-chip training. Realizing a complete fully integrated neuromorphic computing system with low energy consumption and strong learning ability is still in its infancy stage [23-26]. Considering the off-chip training of all the competitors [12-20] is based on software implementation, we mainly compare the computational efficiency of on-chip inference phase. To measure the computational efficiency of the proposed system, a combination of hardware experiments and software simulations is employed in this paper.

1) Hardware experiments

First, we measure the energy efficacy and performance density of the core computing element (i.e., the 2T2M crossbar array implemented by the Au/MSFP/Au memristor), as shown in Table VIII.

TABLE VIII
BENCHMARK METRICS OF THE CORE COMPUTING ELEMENT WITH A 1-BIT INPUT

Metrics	Quantitative value
Area	2.474 μm^2
Power	7.60 pJ/25 ns=0.304 mW
Performance	(24×24×2) ops/(1×25 ns)=46.08 $GOPs^{-1}$
Energy efficiency	46.08 $GOPs^{-1}$/0.304 mW=151.579 $TOPs^{-1}W^{-1}$
Performance density	46.08 $GOPs^{-1}$/2.474 μm^2=18.625 $TOPs^{-1}mm^{-2}$

In this paper, a 24×24 2T2M crossbar array with 28-nm technology is used. The calculation is performed according to the necessary peripheral circuits with 28-nm technology. From Table VIII, we achieve an energy efficiency level of 151.579 $TOPs^{-1}W^{-1}$ and a performance density of 18.625 $TOPs^{-1}mm^{-2}$. The implementation of existing SOH estimation methods

TABLE IX
HARDWARE COMPARISON AMONG THE SOTA CORE COMPUTING ELEMENTS

	Ref. [23]	Ref. [24]	Ref. [25]	Ref. [26]	This work
Technology	40nm	130nm	130nm	14nm	28nm
Memory	1T1M RRAM	1T1M RRAM	1T1M RRAM	2T2M PCM	2T2M ERRAM
Device stability	Unknown	High	High	Unknown	High
Switching type	Analogue	Digital	Digital	Digital	Analogue
Time-frequency domain	No	No	No	No	Yes
Energy efficiency ($TOPs^{-1}W^{-1}$)	75.17	11.01	40.00	10.5	151.58
Performance density ($TOP\ s^{-1}mm^{-2}$)	7.01	1.16	12.80	1.59	18.63
Applications	Unknown	Recognition	Recognition	Recognition	Estimation

This article has been accepted for publication in a future issue of this journal, but has not been fully edited. Content may change prior to final publication. Citation information: DOI10.1109/JIOT.2024.3448350,

[12-20] usually built on the complementary metal oxide semiconductors (CMOS) devices, leading to low energy efficiency and low performance density. For fairness of hardware comparison, a hardware comparison among the neuromorphic computing elements [23-26] is demonstrated in Table IX. Notably, the hardware metrics of the neuromorphic computing elements are excerpted from previous papers [23-26]. Compared with the best metrics of the neuromorphic computing elements (that is, an energy efficiency level of 75.17 $TOPs^{-1}W^{-1}$ and a performance density of 12.80 $TOPs^{-1}mm^{-2}$ with a 1-bit input), the proposed 2T2M crossbar array exhibits an approximately 2.02 times greater energy efficiency level and a 1.46 times greater performance density.

2) Software simulations

Then, the proposed system is simulated in the NeuroSim V3.0 framework [37]. The size of 2T2M array is 128×128. In terms of the device characteristics, the parameters (including the circuit and neural network parameters) used for the proposed time-frequency hybrid neuromorphic computing system are provided in Table II. The time consumption, latency, and power consumption of the proposed system are measured in the NeuroSim V3.0 framework [37]. We analyse the time consumption levels of the on-chip inference process and those of the SOTA methods [12-20] on the two publicly available battery ageing datasets, as shown in Fig. 18.

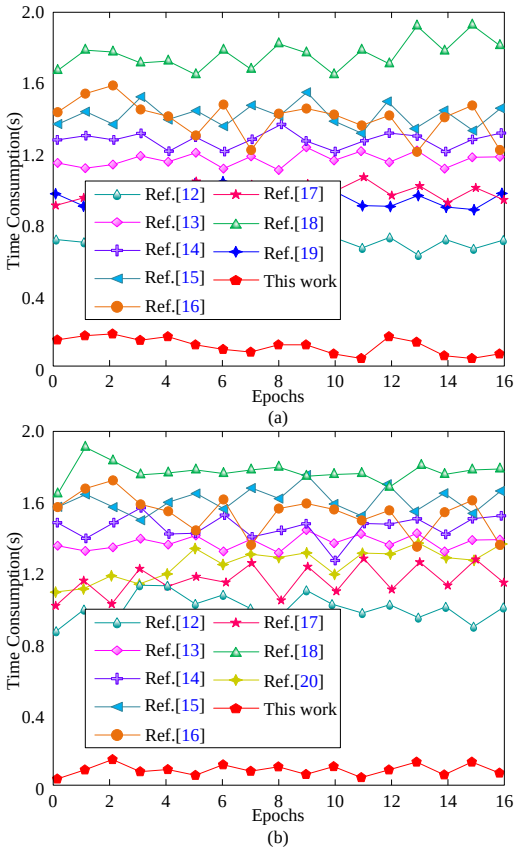

Fig. 18. Time consumption of on-chip inference. (a) CALCE-CS2 dataset; (b) NASA dataset.

According to Fig. 18, the proposed time-frequency hybrid neuromorphic computing system has a significant advantage in terms of time consumption and is approximately 8~12 times faster than the other competitors, satisfying the real-time requirement of the IoT scenario.

Fig. 19 shows the latency breakdown and energy breakdown of the proposed time-frequency hybrid neuromorphic computing system. The energy consumption of the proposed system is measured to be approximately 3606 pJ for 1-bit computing with a 0.7-V, 25-ns read voltage. Among all peripheral circuits, the energy consumption of the ADCs reaches 84.2%, far exceeding that of the core computing elements (i.e., 2T2M crossbar arrays). During the on-chip inference process, the latency of the proposed system is recorded by capturing the duration of the flag signal in the NeuroSim V3.0 framework. The total latency of the proposed time-frequency hybrid neuromorphic computing system is approximately 1.40 ms. Most of the latency is generated by the interconnections among all peripheral circuits. Comparing the metrics attained with an RTX 3090 GPU (that is, a latency of 10.2 ms), the proposed system achieves approximately 10 times faster latency.

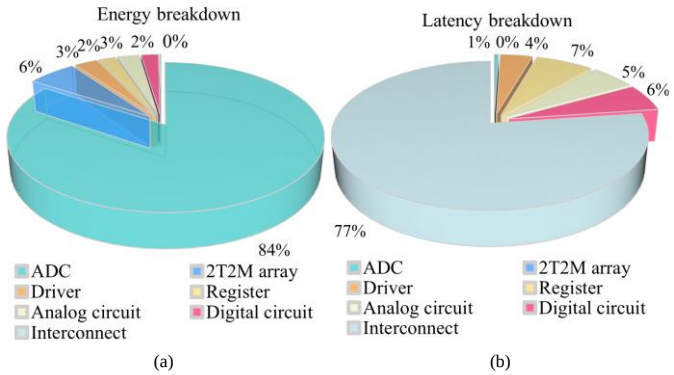

Fig. 19. The breakdown of the time-frequency hybrid neuromorphic computing system by main component (a) Energy breakdown; (b) Latency breakdown.

E. Robustness Analysis

To assess the robustness of the proposed system, a noise-resilient analysis and a device failure analysis are conducted, as illustrated in Fig. 20.

Initially, random noise is introduced to the given electrical signals, comprising voltage, current, temperature, and time data, to verify the robustness of the proposed time-frequency hybrid neuromorphic computing system. The MAEs and RMSEs produced by the proposed system on the CALCE-CS2 dataset and the NASA dataset are depicted in Fig. 20(a). When the level of the random noise is greater than 0.2, a slight reduction is observed in the estimation performance (CALCE-CS2 dataset: −0.11% MAE and −0.10% RMSE; NASA dataset: −0.07% MAE and −0.04% RMSE). The experimental results demonstrate that the impact of random noise on the proposed system can be negligible within a certain range (noise level≤0.2).

Then, to examine the effect of device failure, we set the failure ratio of the memristors in R_{off}/R_{on} from 0% to 30%, and the estimation performances achieved on the CALCE-CS2 dataset and the NASA dataset are illustrated in Fig. 20(b). When the device failure percentage reaches approximately 20%, the estimation performance can be maintained at an acceptable level (CALCE-CS2 dataset: ≤0.25% MAE and ≤0.29% RMSE; NASA dataset: ≤0.26% MAE and ≤0.28% RMSE). Once the

This article has been accepted for publication in a future issue of this journal, but has not been fully edited. Content may change prior to final publication. Citation information: DOI10.1109/JIOT.2024.3448350,

device failure percentage exceeds 25%, the estimation performance significantly decreases on both publicly available experimental battery ageing datasets. The experimental results demonstrate that the proposed time-frequency hybrid neuromorphic computing system exhibits commendable tolerance to device failures.

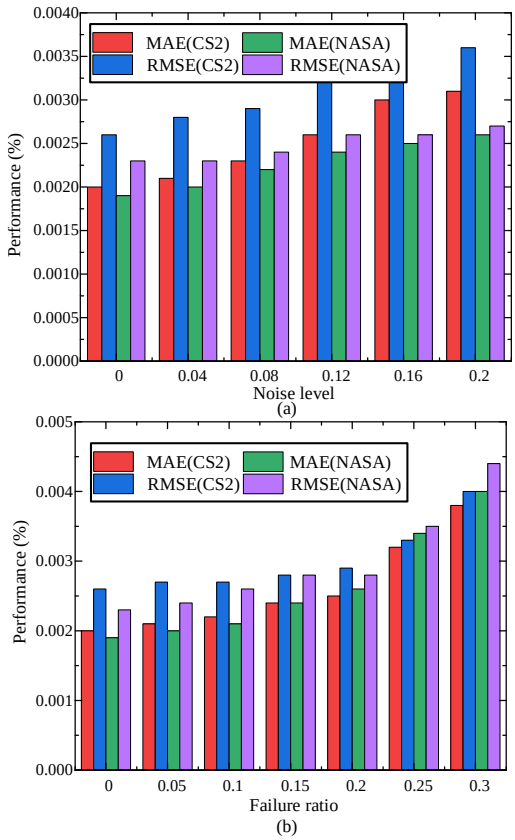

Fig. 20. The robustness analysis of the time-frequency hybrid neuromorphic computing system. (a) Noise-resilient analysis; (b) Device failure analysis.

VI. Conclusion

This paper investigates a time-frequency hybrid neuromorphic computing system for battery SOH estimation. First, an eco-friendly, biodegradable memristor crossbar array is constructed using MSFP-based memristors, which can realize high energy efficiency and high-performance density in the proposed system. Then, the proposed system mainly consists of a local information extraction module, a time-frequency feature fusion module, and a global information perception module. Through the local information extraction module, time-domain features with neighbourhood dependencies can be adequately captured from battery electrical signals. Through the time-frequency feature fusion module, the context information contained in the time domain and the periodic information contained in the frequency domain can be sufficiently exchanged, providing more comprehensive representations for the SOH estimation task. In the global information perception module, global information with long-range dependencies can be extracted, and a reliable output can be effectively obtained. For verification purposes, the proposed system is applied to perform battery SOH estimation tasks on two publicly available battery ageing datasets. Compared with the SOTA methods, the proposed system achieves the best estimation performance and consumes 8~12 times less time. Additionally, a comprehensive computational efficiency analysis and a robustness analysis are conducted, indicating the high computational efficiency and reliability of the proposed system in the IoT scenario.

VII. Discussion

Although the proposed time-frequency hybrid neuromorphic computing system has a capability to process complex electrical signals for battery SOH estimation task, which balances computational efficiency and computing accuracy to promote versatility. The scalability of the proposed system for real-world large-scale applications is still challengeable.

Firstly, almost all the neuromorphic computing systems perform the on-chip inference with high energy efficiency using memristor crossbar arrays although using software operating system to implement the off-chip training. Realizing a complete fully integrated neuromorphic computing system with low energy consumption and strong learning ability is still in its infancy stage. Thus, the hardware implementation of adaptive learning algorithm needs to be further developed in future, which is expected to promote the integration of neuromorphic computing and battery management systems.

Secondly, the development of existing neuromorphic computing systems is limited to specific scenario, and the adaptability requirements of different battery technologies are hard to achieve. Considering the requirements of real-world large-scale application have become more diversified, reconfigurable functional circuits need to be further developed in the future.

Thirdly, the biological interpretability of the proposed time-frequency hybrid neuromorphic computing system is limited. With better understanding of the structure and function of human brain, general learning algorithms for real-time battery SOX estimation including the state of health, state of charge, state of energy, etc. should be studied to promote the development of neuromorphic computing systems for real-world large-scale applications.

References

[1] S. Tao *et al.*, "Collaborative and privacy-preserving retired battery sorting for profitable direct recycling via federated machine learning," *Nat. Commun.,* vol. 14, no. 1, p. 8032, Dec. 2023, doi: 10.1038/S41467-023-43883-Y.

[2] D. Roman, S. Saxena, V. Robu, M. Pecht, and D. Flynn, "Machine learning pipeline for battery state-of-health estimation," *Nat. Mach. Intell.,* vol. 3, no. 5, pp. 447-456, May 2021, doi: 10.1038/S42256-021-00312-3.

[3] J. Bokstaller, J. Schneider, and J. v. Brocke, "Estimating SoC, SoH, or RuL of rechargeable batteries via IoT: A review," *IEEE Internet Things J.,* vol. 11, no. 5, pp. 7559-7582, Mar. 2023, doi: 10.1109/JIOT.2023.3342367.

[4] M. S. Batta, H. Mabed, Z. Aliouat, and S. Harous, "Battery state-of-health prediction-based clustering for lifetime optimization in IoT networks," *IEEE Internet Things J.,* vol. 10, no. 1, pp. 81-91, Jan. 2023, doi: 10.1109/JIOT.2022.3200717.

[5] M. Lin, C. Yan, W. Wang, G. Dong, J. Meng, and J. Wu, "A data-driven approach for estimating state-of-health of lithium-ion batteries considering internal resistance," *Energy,* vol. 277, p. 127675, Aug. 2023, doi: 10.1016/J.ENERGY.2023.127675.

[6] M. Chen, G. Ma, W. Liu, N. Zeng, and X. Luo, "An overview of

data-driven battery health estimation technology for battery management system," *Neurocomputing,* vol. 532, pp. 152-169, May 2023, doi: 10.1016/J.NEUCOM.2023.02.031.

[7] Y. Gao, K. Liu, C. Zhu, X. Zhang, and D. Zhang, "Co-estimation of state-of-charge and state-of- health for lithium-ion batteries using an enhanced electrochemical model," *IEEE Trans. Ind. Electron.,* vol. 69, no. 3, pp. 2684-2696, Mar. 2022, doi: 10.1109/TIE.2021.3066946.

[8] C. Li *et al.*, "SOH estimation method for lithium-ion batteries based on an improved equivalent circuit model via electrochemical impedance spectroscopy," *J. Energy Storage,* vol. 86, p. 111167, May 2024, doi: 10.1016/J.EST.2024.111167.

[9] Z. Xu, J. Wang, P. D. Lund, and Y. Zhang, "Co-estimating the state of charge and health of lithium batteries through combining a minimalist electrochemical model and an equivalent circuit model," *Energy,* vol. 240, p. 122815, Feb. 2022, doi: 10.1016/J.ENERGY.2021.122815.

[10] C. Chang, S. Wang, C. Tao, J. Jiang, Y. Jiang, and L. Wang, "An improvement of equivalent circuit model for state of health estimation of lithium-ion batteries based on mid-frequency and low-frequency electrochemical impedance spectroscopy," *Meas. J. Int. Meas. Confed.,* vol. 202, p. 111795, Oct. 2022, doi: 10.1016/J.MEASUREMENT.2022.111795.

[11] Y. Zheng, J. Hu, J. Chen, H. Deng, and W. Hu, "State of health estimation for lithium battery random charging process based on CNN-gru method," *Energy Reports,* vol. 9, pp. 1-10, May 2023, doi: 10.1016/J.EGYR.2022.12.093.

[12] S. Shen, M. Sadoughi, X. Chen, M. Hong, and C. Hu, "A deep learning method for online capacity estimation of lithium-ion batteries," *J. Energy Storage,* vol. 25, p. 100817, Oct. 2019, doi: 10.1016/J.EST.2019.100817.

[13] B. Liu, J. Xu, and W. Xia, "State-of-health estimation for lithium-ion battery based on an attention-based CNN-GRU model with reconstructed feature series," *Int. J. Energy Res.,* vol. 2023, p. 8569161, Feb. 2023, doi: 10.1155/2023/8569161.

[14] S. Bockrath, V. Lorentz, and M. Pruckner, "State of health estimation of lithium-ion batteries with a temporal convolutional neural network using partial load profiles," *Appl. Energy,* vol. 329, p. 120307, Jan. 2023, doi: 10.1016/J.APENERGY.2022.120307.

[15] L. Chen, S. Xie, A. M. Lopes, and X. Bao, "A vision transformer-based deep neural network for state of health estimation of lithium-ion batteries," *Int. J. Electr. Power Energy Syst.,* vol. 152, p. 109233, Oct. 2023, doi: 10.1016/J.IJEPES.2023.109233.

[16] X. Huang, X. Liu, and Y. Chen, "State of health estimation of lithium-ion battery based on Pre-LN transformer," in *2023 38th Youth Academic Annual Conference of Chinese Association of Automation (YAC)*, Hefei, China, 27-29 Aug. 2023, New York: IEEE, pp. 271-276, doi: 10.1109/YAC59482.2023.10401622.

[17] Y. Yang, S. Chen, T. Chen, and L. Huang, "State of health assessment of lithium-ion batteries based on deep gaussian process regression considering heterogeneous features," *J. Energy Storage,* vol. 61, p. 106797, May 2023, doi: 10.1016/J.EST.2023.106797.

[18] T. Bai and H. Wang, "Convolutional transformer-based multiview information perception framework for lithium-ion battery state-of-health estimation," *IEEE Trans. Instrum. Meas.,* vol. 72, p. 2523312, Aug. 2023, doi: 10.1109/TIM.2023.3300451.

[19] Z. Bao, J. Nie, H. Lin, J. Jiang, Z. He, and M. Gao, "A global–local context embedding learning based sequence-free framework for state of health estimation of lithium-ion battery," *Energy,* vol. 282, p. 128306, Nov. 2023, doi: 10.1016/J.ENERGY.2023.128306.

[20] L. Chen *et al.*, "A new SOH estimation method for lithium-ion batteries based on model-data-fusion," *Energy,* vol. 286, p. 129597, Jan. 2024, doi: 10.1016/J.ENERGY.2023.129597.

[21] F. Aguirre *et al.*, "Hardware implementation of memristor-based artificial neural networks," *Nat. Commun.,* vol. 15, no. 1, p. 1974, Dec. 2024, doi: 10.1038/S41467-024-45670-9.

[22] W. Chen *et al.*, "Essential characteristics of memristors for neuromorphic computing," *Adv. Electron. Mater.,* vol. 9, no. 2, p. 2200833, Feb. 2023, doi: 10.1002/AELM.202200833.

[23] S. D. Spetalnick *et al.*, "A 2.38 MCells/mm^2 9.81 -350 TOPS/W RRAM compute-in-memory macro in 40nm CMOS with hybrid offset/IOFF cancellation and ICELL RBLSL drop mitigation," in *2023 IEEE Symposium on VLSI Technology and Circuits (VLSI Technology and Circuits)*, Kyoto, Japan, 11-16 Jun. 2023, New York: IEEE, pp. 1-2, doi: 10.23919/VLSITechnologyandCir57934.2023.10185424.

[24] P. Yao *et al.*, "Fully hardware-implemented memristor convolutional neural network," *Nature,* vol. 577, no. 7792, pp. 641-646, Jan. 2020, doi: 10.1038/S41586-020-1942-4.

[25] W. Wan *et al.*, "A compute-in-memory chip based on resistive random-access memory," *Nature,* vol. 608, no. 7923, pp. 504-512, Aug. 2022, doi: 10.1038/S41586-022-04992-8.

[26] R. Khaddam-Aljameh *et al.*, "HERMES-Core-A 1.59-TOPS/mm2PCM on 14-nm CMOS in-memory compute core using 300-ps/LSB linearized CCO-Based ADCs," *IEEE J. Solid-State Circuits,* vol. 57, no. 4, pp. 1027-1038, Apr. 2022, doi: 10.1109/JSSC.2022.3140414.

[27] X. Xiang, X. Zhang, and H. Chen, "A convolutional network with multi-scale and attention mechanisms for end-to-end single-channel speech enhancement," *IEEE Signal Process. Lett.,* vol. 28, pp. 1455-1459, Jun. 2021, doi: 10.1109/LSP.2021.3093859.

[28] C. Fan, K. O'Regan, L. Li, E. Kendrick, and W. D. Widanage, "Frequency domain non-linear characterization and analysis of lithium-ion battery electrodes," *J. Energy Storage,* vol. 36, p. 102371, Apr. 2021, doi: 10.1016/J.EST.2021.102371.

[29] Z. Chen, D. Chen, X. Zhang, Z. Yuan, and X. Cheng, "Learning graph structures with transformer for multivariate time-series anomaly detection in IoT," *IEEE Internet Things J.,* vol. 9, no. 12, pp. 9179-9189, Jun. 2022, doi: 10.1109/JIOT.2021.3100509.

[30] G. Zhou *et al.*, "Full hardware implementation of neuromorphic visual system based on multimodal optoelectronic resistive memory arrays for versatile image processing," *Nat. Commun.,* vol. 14, no. 1, p. 8489, Dec. 2023, doi: 10.1038/S41467-023-43944-2.

[31] Y. Wu *et al.*, "Brain-inspired global-local learning incorporated with neuromorphic computing," *Nat. Commun.,* vol. 13, no. 1, p. 65, Dec. 2022, doi: 10.1038/S41467-021-27653-2.

[32] X. Ji, Z. Dong, C. S. Lai, and D. Qi, "A brain-inspired in-memory computing system for neuronal communication via memristive circuits," *IEEE Commun. Mag.,* vol. 60, no. 1, pp. 100-106, Jan. 2022, doi: 10.1109/MCOM.001.21664.

[33] Y. Li, L. Li, R. Mao, Y. Zhang, S. Xu, and J. Zhang, "Hybrid data-driven approach for predicting the remaining useful life of lithium-ion batteries," *IEEE Trans. Transp. Electrif.,* Aug. 2023, doi: 10.1109/TTE.2023.3305555.

[34] F. Naaz, A. Herle, J. Channegowda, A. Raj, and M. Lakshminarayanan, "A generative adversarial network-based synthetic data augmentation technique for battery condition evaluation," *Int. J. Energy Res.,* vol. 45, no. 13, pp. 19120-19135, Oct. 2021, doi: 10.1002/ER.7013.

[35] Z. Dong, X. Ji, J. Wang, Y. Gu, J. Wang, and D. Qi, "ICNCS: Internal cascaded neuromorphic computing system for fast electric vehicle state of charge estimation," *IEEE Trans. Consum. Electron.,* p. Mar., 2023, doi: 10.1109/TCE.2023.3257201.

[36] W. Zhang *et al.*, "Edge learning using a fully integrated neuro-inspired memristor chip," *Science,* vol. 381, no. 6663, pp. 1205-1211, Sep. 2023, doi: 10.1126/SCIENCE.ADE3483.

[37] Y. Luo, X. Peng, and S. Yu, "MLP+NeuroSimV3.0: Improving on-chip learning performance with device to algorithm optimizations," in *Proceedings of the International Conference on Neuromorphic Systems*, Knoxville, TN, USA, 23-25 Jul. 2019, New York: Association for Computing Machinery, p. Article 1, doi: 10.1145/3354265.3354266.